Simulation Framework for Thermal Quasi-Particle Microwave Loss in Multimaterial Superconducting Quantum Circuit Elements

Haoran Duan, Ritika Dhundhwal, Gabriel Cadilha Marques, Dirk Fuchs, Ioan M. Pop, Thomas Reisinger, and Jasmin Aghassi-Hagmann

***Abstract*—Superconducting quantum circuits constitute one of the most advanced and promising platforms for building fault-tolerant quantum computers. However, the associated relatively short coherence times remain a major challenge. Therefore quantifying the various responsible loss mechanisms is key, which can be achieved effectively by refined loss modeling. An important source of dissipation is thermal quasi-particles, for which many simulation tools exist. Here, we improve on these by integrating two of them in a self-consistent manner into an automated workflow for a circuit composed of two materials. Namely, the workflow consists of a numerical simulation of the Mattis–Bardeen surface impedance and electromagnetic finite-element simulation using *Ansys HFSS* to predict temperature-dependent quasi-particle loss from normal state material properties. As a test, we use it to simulate the quality factors as a function of the temperature of superconducting resonators composed of tantalum. Tantalum resonators are often found to be dominated by quasi-particle loss at a significantly lower temperature (less than 1 K) than what would be expected from the bulk critical temperature (4.4 K) observed to good approximation in dc transport measurements. A likely cause is a defect phase with a low critical temperature, potentially associated with the tantalum beta phase. By fitting the temperature-dependent loss data to the workflow results, we estimate the concentration of the defect phase. This is an important step forward in correlating material design and microwave loss.**

***Index Terms*—Simulation framework, superconducting quantum circuits, superconducting resonators, tantalum (Ta), thermal quasi-particle (QP) loss.**

I. Introduction

AMONG the many competitive physical platforms for realizing practical quantum computers, the superconducting quantum circuit [1], [2] is one of the most promising systems with its high gate speed and fidelity, as well as the large scale of qubit integration [3], [4], [5]. In recent years, tantalum (Ta) has attracted widespread interest in the community as an emerging material for superconducting quantum circuit elements. By merely replacing the commonly used niobium with Ta for its capacitor, the coherence time of the transmon qubit is improved by a factor of 3 [6], [7]. This discovery has sparked renewed interest in further improving the coherence of superconducting qubits through materials science [8]. As a natural consequence, superconducting circuits will be increasingly composed of more complex and an increasing number of materials. Consequently, understanding their different contributions to the loss budget of a circuit will be essential. This is the motivation for the simulation framework presented here.

In the last decade, a large number of powerful superconducting quantum circuit design and simulation platforms have emerged. One notable example is Qiskit Metal [9], a powerful open-source quantum electronic design automation. Other *Python* packages for circuit quantum electrodynamics analysis are also available, such as QuCAT [10], SQcircuit [11], and scQubits [12]. All of the aforementioned systems use QuTiP [13], an open quantum system analysis tool, to simulate the dissipation of circuit devices, where a decay rate is required for the dissipation calculation. In general, specific material-dependent superconductivity parameters are not considered in these packages. In the literature on superconducting devices, superconducting material parameters are often introduced into the simulation through the Mattis–Bardeen (MB) model, but they do not take into account the response of more than one material in an automated way [14], [15].

This work was supported in part by the Joint-Lab Virtual Materials Design initiative and the German Research Foundation under Germany's Excellence Strategy via the Excellence Cluster "3D Matter Made to Order" under Grant EXC-2082/1-390761711, in part by the Carl Zeiss Foundation through the "Carl-Zeiss-Foundation Focus @ HEiKA," in part by the State of Baden-Württemberg and Karlsruhe Institute of Technology (KIT), in part by the Federal Ministry of Education and Research and the Ministry of Science, Research and the Arts of Baden-Württemberg, as part of the National High-Performance Computing joint funding program (NHRKIT) for carrying research at National High-Performance Computing Center, KIT, and in part by the German Research Foundation for using high-performance computer HoreKa. The work of Ritika Dhundhwal, Ioan M. Pop, and Thomas Reisinger was supported in part by the Helmholtz Association, in part by the European Union's Horizon 2020 research and innovation program through the Marie Skłodowska-Curie Grant under Grant 847471, in part by the Helmholtz Programm MSE, joint Lab VMD is acknowledged, and in part by the Federal Ministry of Education and Research through Project GeQCoS under Grant FKZ:13N15683. *(Corresponding author: Jasmin Aghassi-Hagmann.)*

Haoran Duan, Gabriel Cadilha Marques, and Jasmin Aghassi-Hagmann are with the Institute of Nanotechnology, Karlsruhe Institute of Technology, 76131 Karlsruhe, Germany (e-mail: jasmin.aghassi@kit.edu).

Ritika Dhundhwal, Dirk Fuchs, and Thomas Reisinger are with the Institute of Quantum Materials and Technologies, Karlsruhe Institute of Technology, 76131 Karlsruhe, Germany.

Ioan M. Pop is with the Institute of Quantum Materials and Technologies, Karlsruhe Institute of Technology, 76131 Karlsruhe, Germany, also with the Institute of Physics, Karlsruhe Institute of Technology, 76131 Karlsruhe, Germany, and also with Physics Institute 1, University of Stuttgart, 70569 Stuttgart, Germany.

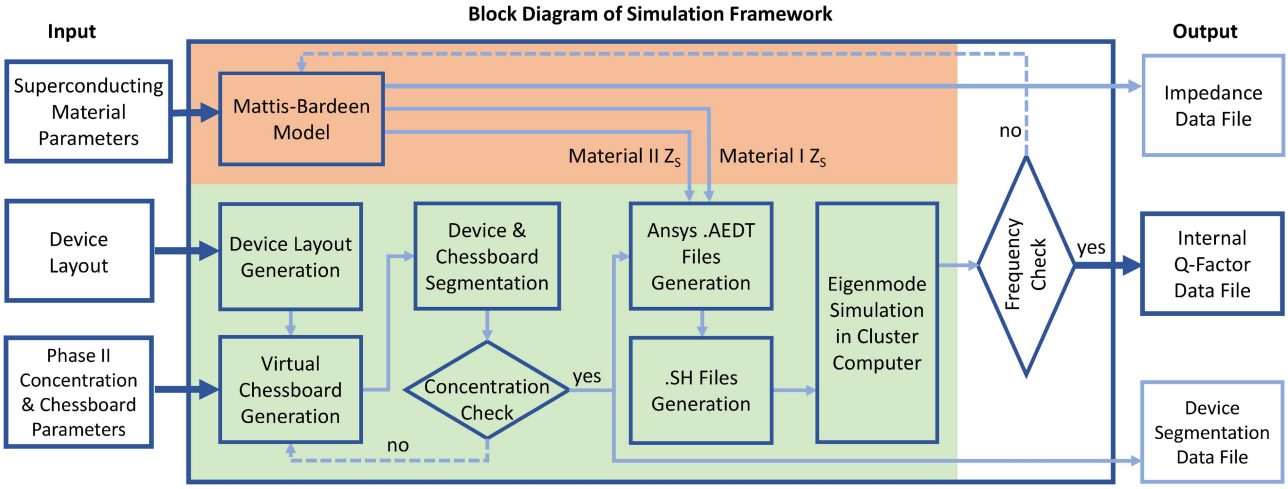

Fig. 1. Conceptual block diagram of the entire framework and simulation framework for thermal QP loss in superconducting resonators composed of two materials to predict their temperature-dependent quality factors. Input parameters include superconducting material parameters, temperature and frequency ranges, dimensions of device layout, and parameters relating to the spatial distribution of the second phase. The automation of the superconducting device layout generation and segmentation for the phase distribution is accomplished by *PyAEDT*. Surface impedances computed using the MB model (highlighted in orange) are set as boundary conditions of different phases for the *HFSS* eigenmode simulation. Generation of the simulation files (one for every surface impedance) and the extraction of simulation results from *HFSS* files is carried out on a local computer, while the eigenmode simulation can be parallelized on an HPC platform. The part of the framework highlighted in green color is using *Ansys HFSS* via *Python* package *PyAEDT*. In the output area, the main output is highlighted in dark blue box, and the intermediate data of the simulation are marked in light blue box.

As a step in this direction, we present a simulation framework and a workflow that integrates the latter in a self-consistent manner with the electromagnetic simulation software *Ansys HFSS* to predict thermal quasi-particle (QP) loss in superconducting resonators composed of two materials. We use the surface impedance boundary condition (SIBC) based on MB theory, which assumes that thickness and curvature radius of the devices are larger than the magnetic field penetration depth. It reduces requirements on computing resources when compared to the more accurate complex conductivity [15] and intrinsic impedance [16] methods, which require the solver to solve Maxwell's equations in the entire volume of the device.

Superconducting quantum circuits are generally not operated at temperatures where thermal QP loss is relevant. However, temperature-dependent loss is a convenient way to examine the superconducting properties of the circuit materials and possible degradations of it. We consider this scenario in a test application for the presented framework. Finally, other example applications of this framework include the simulation of thermal QP loss in superconducting radio frequency devices [17] or circuits composed of multiple elements with different superconducting properties, such as QP-engineered devices [18] or circuits composed of metal alloys that phase separate [19], [20].

The rest of this article is organized as follows. We start by introducing the two methods employed by the workflow. First, MB theory is presented in Section II-A with a brief historical account and a discussion of the input parameters and limitations of the model. In Section II-B, we introduce the architecture of the *Ansys HFSS* part of the simulation framework and explain in detail the implementation of the self-consistent inclusion of two materials. In Section III, we then demonstrate an example application of the workflow by simulating loss in superconducting resonators composed of Ta with defects as the second material. Finally, Section IV concludes this article and provides an estimate for the defect concentration in the Ta resonators as well as a brief outlook.

II. Methods of the Simulation Framework

The framework presented here aims to simulate the temperature-dependent thermal QP microwave loss of the superconducting circuit elements composed of two materials. A detailed diagram of the general workflow based on this framework to fulfill the goal can be found in Appendix A. In addition, the thermal QP results in a shift of the resonance to lower frequencies, which can also be modeled with this framework. However, here, we choose to focus on loss as the relative frequency shifts are normally small and, therefore, harder to simulate accurately (see Appendix B). On the top level, the framework consists of two main parts (see Fig. 1), which are described in the following two sections.

A. MB Theory

In the first part of the framework highlighted in orange in Fig. 1, we determine the surface impedance $Z_s(T, f) = R + iX$, where R is the surface resistance and X is the surface reactance of the two superconducting materials for a list of temperatures T and frequencies f. Each material is defined by a set of five material parameters, as discussed later. For these calculations, we employ a program written by Halbritter [21] around 1970, which solves the microscopic electromagnetic response of a superconductor based on the Bardeen–Cooper–Schrieffer (BCS) theory [22] (see Appendix C). We start with a short recap of the literature leading up to Halbritter's code and

then discuss its limitations. Finally, we discuss the material input parameters, summarizing some equations to estimate them.

Mattis and Bardeen [23] derived the first microscopic electromagnetic response model of superconductors from BCS theory soon after the latter was published. By considering the extreme anomalous limit, where the electron mean free path $l \longrightarrow \infty$, and London penetration depth is smaller than the coherence length $\lambda_L < \xi_0$, they derived an expression for the ratio of complex conductivity for the superconducting state $\sigma_s = \sigma_1 + i\sigma_2$ to normal conductivity σ_N. In principle, the expression given there can be solved numerically. Converting it to a surface impedance, as required for the *HFSS* simulation software, is not straightforward in general, but in the extreme anomalous limit [14], it is approximately given by $Z_s(T) = A\sigma_s(T)^\gamma$, where A is a constant and $\gamma = -1/3$. However, the accurate numerical solution of MB model is difficult, and the expression does not take into account the electron mean free path. In subsequent developments in the community, the model was improved, making it more practical for simulating real superconducting materials [24], and expanding the microwave absorption frequency beyond the superconducting energy gap $\Delta(0)$[25].

Meanwhile, Abrikosov et al. [26] derived an expression of the superconducting current density based on the BCS Hamiltonian and the quantum field method, conveniently introducing the mean free path of electrons in the material as a parameter. Following the field method, Halbritter [21], [27] developed a surface impedance model with an accessible Fortran implementation. For the framework presented here, we take advantage of Halbritter's work and convert the original Fortran code into *Python* to make it more accessible to the quantum computing community. For convenience, we will refer to it as the MB model in the rest of this paper.

Note that the MB model requires the following basic assumptions to be true. First, it is intrinsically only applicable to weakly coupled superconductors since it is a derivative of the BCS theory. Second, it is only applicable to low-field-strength ($H \ll H_c$) and low-frequency ($\hbar\omega \ll \Delta_0$) conditions. Fortunately, the aforementioned conditions are met for most application scenarios of superconducting quantum computing devices.

There are seven input variables to the MB model in total. Out of these two are environmental variables, namely, temperature T and frequency $\omega/2\pi$. The other five are parameters relating to the superconductivity of the material: critical temperature T_c, superconducting bandgap $\Delta(0)$, coherence length ξ_0, London penetration depth λ_L, and the charge carrier mean free path l. The latter four are all considered at 0 K. The output of the model includes surface resistance R_S, surface reactance X_S, and penetration depth at finite temperature λ_T, which is related to the surface reactance by $X_S = \omega\mu_0\lambda_T$.

B. 3-D Finite-Element Electrodynamics Simulation

In Fig. 1, the second part of the framework is highlighted in green. It contains the 3-D finite-element electrodynamics eigenmode simulation of the resonators in *HFSS*, which are used to determine resonator quality factors for the temperature- and frequency-dependent boundary conditions determined in the previous section. The impedance values are fed into multiple *HFSS* simulation files that can be solved in parallel in a high-performance computing (HPC) environment. This part of the framework is automated by the *PyAEDT*, a Python client library that interacts directly with the *Ansys Electronics Desktop* (AEDT) application programming interface (API). Next, we will give a more detailed description of the *PyAEDT*-based components of this simulation framework. We will introduce them in the approximate order in which they are called in the workflow.

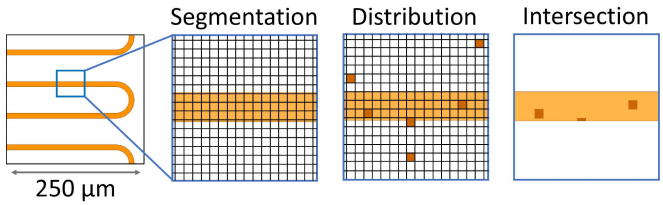

Fig. 2. Implementation of randomly distributed defects as the second material in the *HFSS* simulation using a chessboard grid. The left-most image shows a section of the lumped element resonator schematic. Next to it is a magnified schematic showing a small portion of the meandered inductor with the chessboard-like grid array used for uniformly distributing the low-T_c phase at random and at the required concentration, as shown in the adjacent image to the right. Here, the concentration of defects is set to be 6%, and the width of each grid cell is set to 3 μm, for illustration. Finally, via an intersection operation between the resonator and the selected defect grid cells, the device layout with two materials is formed. To this, we apply the two different impedance boundaries as determined from the MB model calculations.

As a first step, the workflow generates a template file (*.aedt*) for the *HFSS* simulation. It contains the device layout design with two materials, where the secondary material is homogeneously distributed throughout the primary material. There are various ways to enter the device layout into *HFSS*. In the workflow, we give the option to import either an external *.gds* file or create the layout for a particular lumped element resonator directly using the *PyAEDT* package. This defines the areas covered by the primary material. Note that in the simulation, the electromagnetic response of the superconducting circuit device is described by the SIBC neglecting the thickness. The method for embedding the secondary material regions homogeneously in the same area is shown schematically in Fig. 2: The workflow first divides the surface containing the circuit into a regular chessboard structure. In *PyAEDT*, we realize this by creating a virtual grid array. We then select a number of grid elements corresponding to the secondary phase concentration at random. Using 2-D sheet objects in *PyAEDT*, the workflow segments the original device layout, resulting in two objects corresponding to the two materials. There will be a certain deviation between the generated concentration and the required concentration, due to the finite size of the grids and the distribution of the secondary material across the full surface. There is a checking procedure in the workflow that determines how large this deviation is and decides if it is too large. A threshold for this deviation can be set as an input parameter together with the size of the grid elements. Finally, the workflow applies all the general simulation settings

to the template file. Template files for the example application of the simulation framework can be found in Appendix G.

Once the template *.aedt* file is finalized, the workflow duplicates it as needed and sets the impedance boundary condition calculated by the MB model corresponding to each temperature (and frequency). The advantage of generating a separate file for every temperature is that the files can be solved in parallel on different machines or in a cluster computing environment. To simplify this, the workflow automatically generates a shell script file (*.sh*) related to each *.aedt* file. A batch file also implemented as shell script is generated, which can be executed to submit all *.aedt* files to the cluster computing environment at once.

In the next step of the workflow, the simulation files are executed in an HPC environment. In the workflow application discussed below, the simulations are performed on either BwUniCluster2.0 or HoreKa. Both use the Simple Linux Utility for Resource Management to schedule jobs. Before their execution, the generated files need to be uploaded from the local computer to the HPC. To achieve this as well as downloading the solution files after execution, the workflow uses the Secure Shell package. The code for uploading, executing, and downloading is contained in the Python script of the workflow. Finally, after downloading the results, the workflow can be used to extract the eigenfrequencies and quality factors from *HFSS* result files and plot them.

Note that the device frequency is both an input of the MB model and an output of the *HFSS* eigenmode simulation. Therefore, the workflow includes an optional loop that approaches self-consistent frequency values. When the self-consistent loop mode is turned ON, for each temperature, the workflow generates a set of surface impedances within a certain input frequency range, which is written in the *Optimetrics* option of the corresponding *.aedt* file. In this case, the workflow will try to find an interpolated match between input and output frequencies for each temperature. The frequency determined in this way is then used in the next loop iteration. The loop mode is particularly useful if the superconducting material has high kinetic inductance, such as in the case of disordered superconductors [28]. We would like to emphasize for clarity that the workflow does not predict some sources of loss commonly encountered in microwave devices, such as those resulting from dielectrics, local field enhancements, or nonideal (rough/disordered) boundaries, which normally only exhibit a weak temperature dependence. A short discussion of current crowding and local field enhancements is found in Appendix F.

III. Example Application of the Simulation Framework

An example application of the simulation framework is presented in Fig. 3. Our test device for the framework is a superconducting lumped element resonator shown schematically in Fig. 3(b) and composed of Ta as a superconducting material. In experiments, we and other groups [29] found an unexpectedly low superconducting T_c as deduced from temperature-dependent quality factor measurements ($RF - T_c$), when compared to four-point-probe transport measurements (performed in a Quantum Design physical property measurement system)

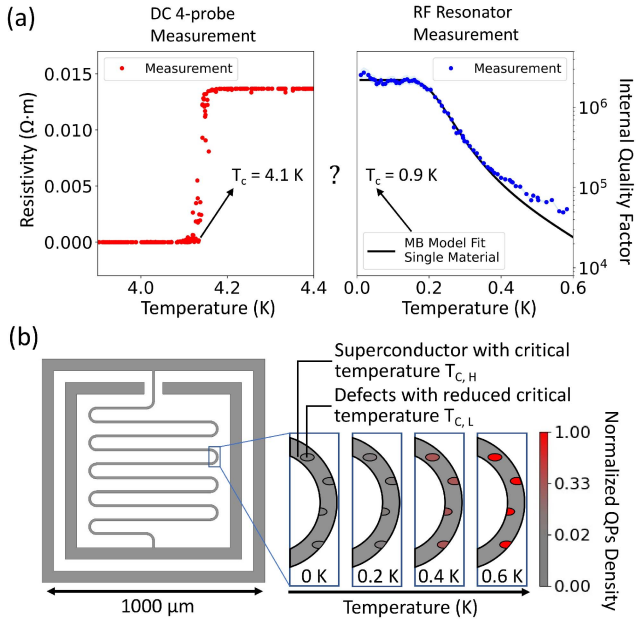

Fig. 3. Example application and motivation for the multimaterial simulation framework. (a) Discrepancy in critical temperature measured with dc transport and inferred from microwave resonator loss. The left-hand graph shows the resistivity of a Ta thin film as a function of temperature measured with the four-probe technique in a physical property measurement system. There is a clear superconducting transition at the indicated temperature T_c. The right-hand plot shows the internal quality factor as a function of the temperature of lumped element resonators patterned from the same film. T_c can be determined from these measurements by fitting the decrease in quality factor as temperature increases with a model for thermal QP loss (Halbritter's implementation of the MB theory—see text). A possible origin for the clear discrepancy in the T_c values is explained in (b), where low-T_c defects are contained in the film. The left schematic shows the lumped element Ta resonator used for the microwave loss measurements. It is composed of Ta on sapphire lithographically shaped into a meandered inductive part that connects two outer square-shaped capacitor plates. The eigenfrequency of the Ta resonator is 5.5 GHz. The series of magnified images of the meander indicate the exponential increase in QP density at randomly located defects causing microwave loss, while the defects have a sufficiently low concentration to be shorted out in dc measurements. Here, the critical temperatures of tantalum $T_{c,H}$ and for the elliptical defects $T_{c,L}$ are set to 4.4 and 0.6 K, respectively. The color scale is normalized by the thermal QP density of the defect at 0.6 K. The size of the defects is exaggerated for clarity.

of the Ta films used for patterning the resonators [see Fig. 3(a)]. The latter are close to the value $T_c = 4.4$K for bulk Ta [30]. We determined the Ta resonator quality factors, by placing the sapphire chips with the patterned resonators in a waveguide, that was attached to the mixing chamber stage of a dilution cryostat, and measuring microwave reflection coefficients near the resonance frequency as a function of temperature. The measurement uncertainty from Fano interference [31] is less than the marker size. T_c can be determined from these measurements by fitting the decrease in quality factor as temperature increases with the MB model for a single material and $Q_{\mathrm{MB}} = \frac{1}{\alpha} X/R$, where α is the kinetic inductance ratio, which is also varied in the fit, giving $\alpha = 0.001$. The fit takes into account a temperature-independent residual loss term Q_o, which could be, for example, associated with dielectric loss, giving a total quality factor $1/Q_{\mathrm{total}} = 1/Q_o + 1/Q_{\mathrm{MB}}$. Details of the measurements can be found in [32].

TABLE I
SUPERCONDUCTING PARAMETERS OF TANTALUM FILMS COLLECTED FROM LITERATURE COMPARED TO THE DERIVED VALUES USED IN THIS ARTICLE

References	T_c (K)	Δ_0/kT_c	λ_L (nm)	ξ_0 (nm)	l_0 (nm)
this work	4.4	1.8	22	205	60
[39]	4.46	1.775	35	93	n/a
[40]	4.44	n/a	100	30	82
[41]	4.25	n/a	90	54	10

A straightforward explanation for this discrepancy is that the RF $-$ T_c measurements are sensitive to small concentrations of low-T_c material in the resonator [see Fig. 3(b)], because the RF currents in the resonator split between the two Ta phases proportionally to their microwave impedance. In contrast, a subpercolation concentration of a reduced T_c phase will be shorted out and invisible in dc transport. If the defects are sufficiently small-grained and sparse, they can easily evade detection in X-ray-diffraction (XRD) analysis and transmission electron microscopy. While the low-T_c material could be, for example, associated with impurities introduced during fabrication, it is likely that the defects are composed of the Ta β phase, which has a lower T_c compared to the bulk Ta α phase [29], [33], [34] found in film characterization and, therefore, results in excess thermal QP loss with temperature. By fitting the results of the workflow to measured resonator quality factors as a function of temperature, we estimate a concentration of low-T_c material that would have to be present to incur the observed loss.

First, the input parameters for the example application of the workflow need to be determined. There is abundant literature exploring the superconductivity parameters of Ta, some of which are listed in Table I. However, we decided to use the simple following simple approximations to determine them from room temperature properties of Ta. The three length scales λ_L, ξ_0, and l can be estimated from mass m and charge e of the charge carriers, their number density N_0, and room temperature conductivity σ_n. Note the simple estimate $N_0 = \rho N_A/M_{\text{mol}}$, with density ρ, Avogadro number N_A, and the molar mass M_{mol}. The London penetration depth can be approximated using the equation $\lambda_L = \sqrt{m/(\mu_0 N_0 e^2)}$[35]. The BCS coherence length we estimate with $\xi_0 = v_f\hbar/\pi\Delta_0$[30], where $v_F = \frac{\hbar}{m}(3\pi^2 N_0)^{1/3}$ is the free-electron Fermi velocity. Note that the coherence length used in the MB model ξ_{MB} has a relationship with BCS coherence length $\xi_{\text{MB}} = \frac{\pi}{2}\xi_0$ [36]. In the workflow, we estimate the elastic scattering mean free path of charge carriers l_0 at 0 K with the room temperature charge carrier mean free path l_n multiplied by the residual resistance ratio. Finally, l_n can be estimated using the Drude model expression $l_n = \sigma_n m\nu_F/(N_0 e^2)$[30]. The input parameters used in the work flow are $T_c = 4.4$ K [30], $\sigma_n = 7.6 \times 10^6$ S $\cdot$ m^{-1} [37], $\rho = 16.65$ g $\cdot$ cm^{-3} [37], and $M_{\text{mol}} = 180.95$ g $\cdot$ mol^{-1} [37]. The resulting superconducting parameters are summarized in the first line of Table I. Sensitivity of surface impedance to the three length parameters can be found in Appendix D.

The use of the SIBC based on MB theory for finite-element method simulation imposes restrictions on the device geometry, namely, that the thickness and curvature radius of the device be larger than the magnetic field penetration depth $\lambda(\omega, T)$ [16]. This is because the MB surface impedance model is derived based on the assumption of a semi-infinite superconductor. A model for a corrected effective surface impedance can be found in the literature [38]. In the example application, the resonator thickness is approximately 250 nm, while the MB model calculates $\lambda(\omega, T)$ values of 55–100 nm over the temperature range of 0–0.59 k at 5.5 GHz. The resulting correction factors for the surface impedance are, therefore, expected to be small and are not included in the presented simulation results. Furthermore, conforming with the restriction on lateral dimensions, we assume that the defect phase is composed of rectangular blocks with a radial dimension of at least 1 μm (see Appendix G) that penetrate the film. The actual distribution is not known for the film.

Out of the considered input parameters, the superconducting gap $\Delta(T)$ has the strongest influence on the temperature-dependent microwave loss of a superconducting device. When only the BCS superconducting mechanism is considered, the energy gap ratio Δ_0/kT_c of weakly coupled superconductors is then a constant (the so-called BCS constant) [30], and the temperature characteristics of the superconducting energy gap are completely determined by T_c. Therefore, in the actual simulation of Ta resonators, we only use different T_c to distinguish different phases of Ta materials while keeping other input material parameters fixed. More specifically, we fix all material parameters of the resonator except T_c of the defect phase and its concentration, which are obtained by fitting the result of the workflow to the experimental data.

In order to test the workflow, we applied it to the example application described earlier for a large range of defect phase concentrations C_L and critical $T_{c,L}$. The result is shown in Fig. 4. Note that the workflow does not take into account any proximity effect [42], [43] between the majority and the defect phase. In the case of the Ta resonator considered here, we expect this to be a reasonable assumption: The critical temperature of the defect phase as derived from thermal QP loss is significantly lower than the critical temperature measured in dc transport and that of α phase Ta. The defect phase likely has a poor interface with the majority alpha Ta phase in this case. In a different Ta resonator discussed in [32], which has a β phase component detectable in XRD, the critical temperature is not reduced nearly as much, which hints at a stronger proximity coupling between the two phases. As a consequence of neglecting the proximity effect, the quality factor can only be calculated up to T_c of the defect phase. Furthermore, the graphs illustrate that defect phase concentration and critical temperature are correlated to some extent, limiting the accuracy with which the defect phase concentration can be determined.

We also fit the quality factor measurements shown in Fig. 3(a) to lift the discrepancy with dc transport measurements. The result is shown in Fig. 5. We deduce that the measured temperature dependence of the resonator quality factors is compatible with a concentration of a few percent of the defect phase. This extracted

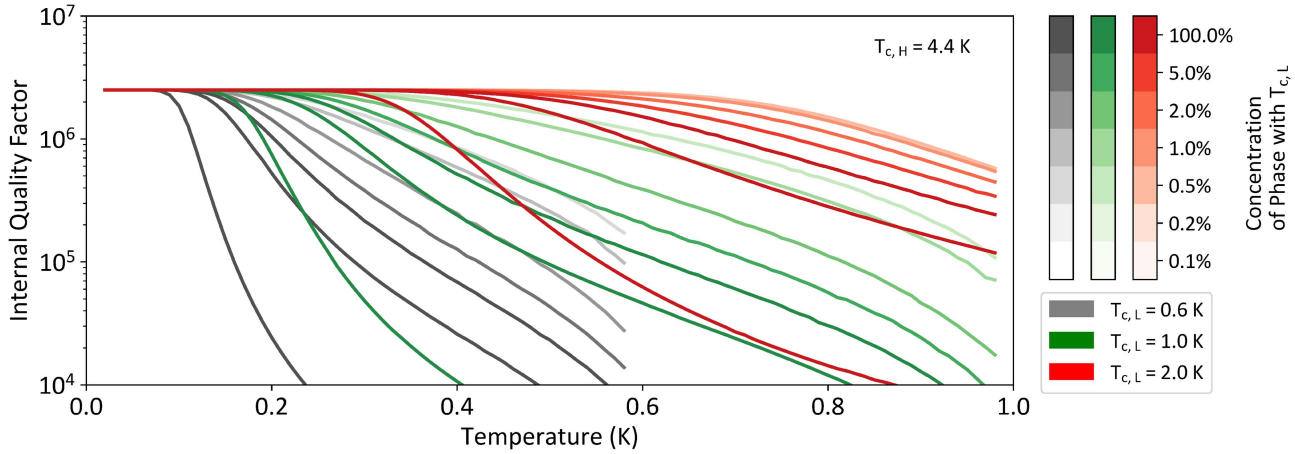

Fig. 4. Simulated internal quality factors of the lumped element Ta resonators calculated with the workflow for different concentrations C_L and critical temperature values $T_{c,L}$ of the defect phase. The defect phase is assumed to be embedded in α phase Ta with critical temperature $T_{c,H} = 4.4$ K. The constant residual loss Q_o at low temperature we set to 6.25×10^6, as it roughly corresponds to the low temperature loss observed in Ta-based devices. The graphs show that the lower the $T_{c,L}$ of the defect phase, the more significant the effect of the defect phase concentration C_L is on the quality factor curve. The resonator structure simulated in this quality factor map is shown in the lower left corner. Note there is a slight difference compared to resonators shown in Figs. 3 and 5.

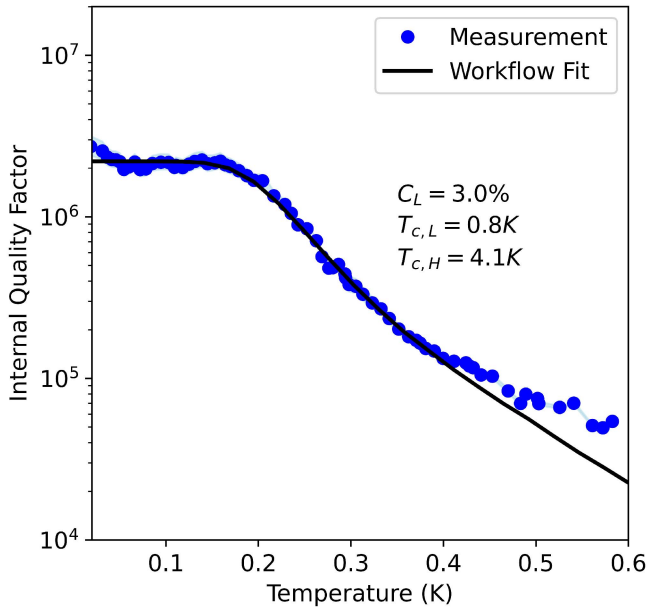

Fig. 5. Simulation workflow applied to the Ta resonator internal quality factor measurement, also shown in Fig. 3. We adapt the defect concentration C_L and critical temperature $T_{c,L}$, while keeping $T_{c,H}$ fixed at the values measured in four-point-probe measurements. Other material parameters in the simulation are fixed and the values are shown in Table I. The resulting value for $T_{c,L}$ is very similar to the one extracted with the single-phase model. However, the workflow model predicts that defect concentrations as small as $C_L = 3\%$ are sufficient to explain the observed loss. Note that at this level of concentration, the defects can be completely shorted in dc four-point-probe measurements, while the low $T_{c,L}$ results in defects dominating the loss characteristics in microwave measurements.

volume concentration is below the percolation threshold, which is typically between 10% and 30% [44], [45], and therefore compatible with the higher critical temperatures observed in dc transport four-probe measurements if uniformly distributed. Note that, in XRD, there is no evidence for the presence of any β-phase Ta in the particular sample (see Appendix E). However, considering the small concentration, the β-phase crystallites are likely too small to detect with this method. Similarly, they could also easily evade detection in localized techniques such as transmission electron microscopy, depending on how homogeneously they are distributed. High-resolution scanning techniques, such as electron-back-scatter-diffraction or synchrotron-based XRD, are more likely to be successful in confirming the presence of these defects.

IV. Conclusion

The presented simulation framework and workflow (depicted schematically in Appendix A, Fig. 6) provide a solution for modeling thermal QP loss in superconducting circuit devices composed of two superconducting materials. It is based on a numerical simulation of the MB surface impedance, with the results entered into *Ansys HFSS* models via the *Python* module *PyAEDT*. These models are solved in parallel in an HPC environment, and the extraction of the results is automated.

We test the simulation workflow by fitting the measured temperature dependence of microwave loss in superconducting Ta resonators. We propose that the losses are dominated by a defect phase with depressed T_c and predict a defect concentration. The latter is of the order of a few percent and, therefore, explains why T_c measured in dc four-point-probe measurements is significantly closer to that of bulk Ta.

In addition to modeling defect concentrations, we expect that this framework and workflow can be applied to the simulation of temperature-dependent microwave losses of other superconducting circuit devices composed of multiple superconducting phases, for example, due to the use of different materials, phase separation in alloys, or variations in thin film thickness. Future extensions to the simulation framework could, for example, incorporate the loss from surface dielectrics via an effective surface resistance [46].

APPENDIX A
DETAILED WORKFLOW DIAGRAM

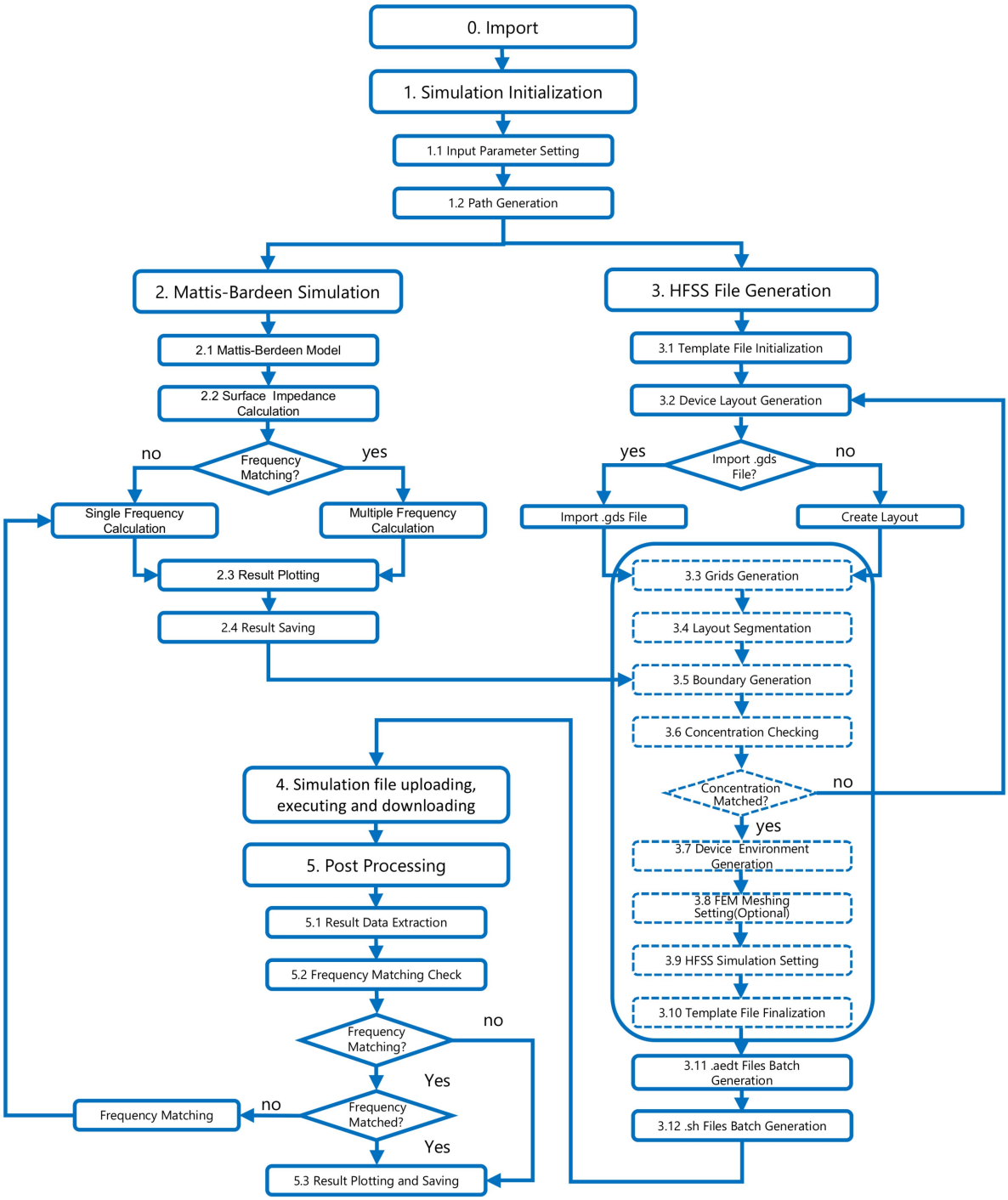

Fig. 6. Detailed workflow program diagram for general simulation applications. The program implementing the workflow is divided into five parts as can be seen in Fig. 6. Each large box explains the function of one main part, and each smaller box represents a cell in a Jupyter Notebook. The Python notebook implementing the workflow can be found on GitHub (https://github.com/HRD1103/Mattis_Bardeen_HFSS_Workflow).

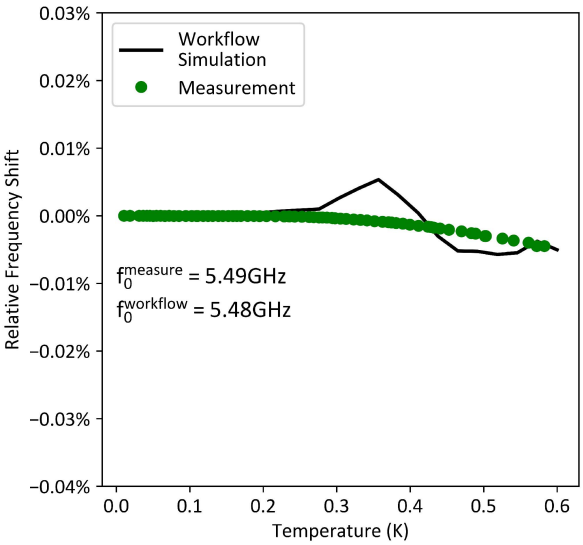

Fig. 7. Simulated temperature-dependent relative frequency shift using the workflow. f_0^{measure} and f_0^{workflow} are the frequencies at the initial temperature of the measured data and the workflow simulation result, respectively. The difference between the two frequencies may come from the slight difference between the actual geometry of the tested device and the designed geometry due to the manufacturing process, as well as the 2-D approximation of the device during the simulation process. The simulation curve is smoothed using the exponentially weighted moving average method.

Appendix B
Frequency Shift

The temperature-dependent frequency shift due to thermal QPs is not discussed in the main text. For completeness, we document here the workflow simulation result for the frequency shift corresponding to the quality factor data in Fig. 5. The relative frequency shift simulated with the workflow is shown in Fig. 7 and compared to the measured resonator frequency as a function of temperature. As can be seen, the simulation exhibits fairly large fluctuations compared to the small frequency shift measured. To save computing resources, we did not pursue the aim of making the results more accurate. This could be achieved by a more stringent termination condition for the frequency change between two iterations in the *HFSS* simulation—for the simulation result shown, this was 1% . With this setting, each simulation job corresponding to a single *.aedt* file and a specific temperature used 179 MB of RAM and 4 h of computing time in the cluster computer.

Appendix C
Surface Impedance Model

Halbritter's [21] surface impedance model is employed for the workflow impedance boundary calculation. A detailed discussion of the model and the employed numerical integration methods can be found in [27]. Under the condition of diffuse electron surface scattering, the surface impedance can be expressed as

$$Z_S = i\mu_0\omega\pi\lambda_L \frac{1}{\kappa \int_\infty^0 dq \frac{\ln(1+Q(q,\omega))}{|Q(0,\omega)|\kappa^2 q^2}} = R_S + iX_S. \quad (1)$$

In this formula, ω is the electromagnetic field frequency, $\lambda_L = \frac{1}{\sqrt{\mu_0|Q(0,\omega)|}}$ is the London penetration depth at zero temperature, and $Q(q,\omega)$ is the MB kernel, the detailed form of which is given in (2). In the dimensionless parameter $\kappa = \frac{\lambda_L \Delta(T)}{\xi_F \Delta(0)}$, where the model input parameter ξ_F is the Cooper pair coherence length, $\Delta(T) = \Delta(0)\sqrt{\cos(\frac{\pi}{2}(\frac{T}{T_c})^2)}$ is the temperature-dependent superconducting gap, where the model input parameter T_c is the critical temperature.

When calculating the Q integral, the integral variable q is replaced by k using $k = \frac{q\Delta(T)}{\xi_F \Delta(0)}$. $Q(k,\omega)$ is divided into three parts, where $Q_A(k,\omega)$ and $Q_P(k,\omega)$ are real and represent surface reactance, which are the electromagnetic response of the Cooper pairs, and $Q_{\text{SCH}}(k,\omega)$ is imaginary and represents surface resistance, which is the electromagnetic response of the Bogoliubov QP

$$Q(k,\omega) = \frac{1}{\mu_0\lambda_L^2}\left(Q_A(k,\omega) + Q_P(k,\omega) + Q_{\text{SCH}}(k,\omega)\right). \quad (2)$$

Appendix D
Sensitivity of Surface Impedance to Length Parameters

We calculate the dependence of MB surface impedance on three length parameters, namely, London penetration λ_L, coherence length ξ_0, and electron mean free path l_0, which are shown in Fig. 8. Here, the surface resistance R_S is taken from the real part of the MB surface impedance, and the quality factor is calculated as the surface quality factor, which is the ratio between the surface reactance and the surface resistance $Q_S = X_S/R_S$.

Appendix E
X-Ray Diffractogram of the Ta Film

In this appendix, we present the crystallographic analysis of the Ta thin film, deposited by magnetron sputtering, and used to fabricate the superconducting resonator shown in Figs. 3(a) and 5 in the main text. We use a Bruker high-resolution XRD system in reflection, equipped with a (0 2 2) Ge monochromator for the characteristic K_α line of a Cu X-ray source. As can be seen in Fig. 9, there are no peaks corresponding to β-phase Ta or any other impurity phases. The small sharp satellite peak at 34.7° close to the Ta $\alpha(110)$ peak, is due to some remaining Cu K_β X-rays not filtered out by the monochromator.

Appendix F
Field Enhancement and Current Crowding

Local field enhancement and current crowding are common physical effects in microwave devices. Both effects can be correctly described by *Ansys HFSS* as long as the final mesh has sufficient resolution in the relevant volume. In this simulation framework, the losses caused by current crowding are included in the simulation calculation based on SIBCs of the metal parts. Since the loss tangent of the dielectric material is not included in the simulation parameters, this workflow cannot simulate the losses caused by local field enhancement; this part of losses are

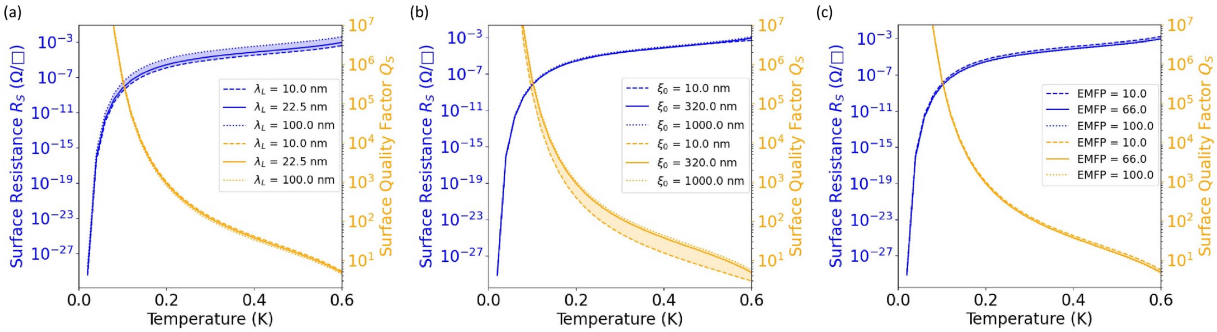

Fig. 8. Sensitivity of MB surface impedance to three length parameters λ_L, ξ_0, and l_0. Here, we used the curve of beta phase Ta as a baseline, with the material parameters are $T_c = 0.6$ K, $\Delta_0/kT_c = 1.8$, $\lambda_L = 22$ nm, $\xi_0 = 320$ nm, and $l_0 = 60$ nm, which are the values used in the example application in Section III. We sweep the three length parameters over the range of one order of magnitude to observe the sensitivity of the surface resistance R_S and the surface quality factor Q_S to these parameters. These results show that the range of variation of R_S and Q_S is significantly smaller than the range of variation of the input length parameters.

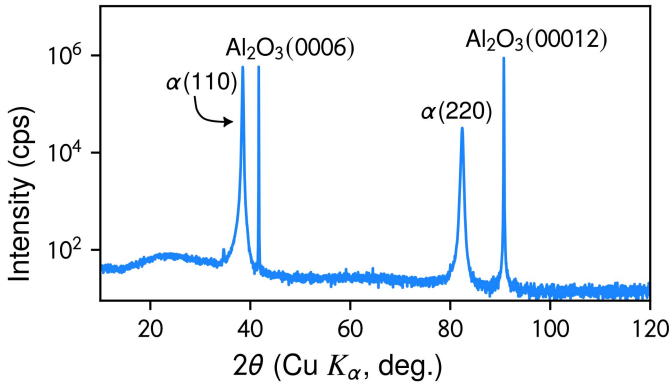

Fig. 9. XRD data of Ta thin film grown on c-plane Al_2O_3. The diffractogram shows two sharp substrate peaks corresponding to c-plane sapphire and two Ta peaks, denoted $\alpha(1\,1\,0)$ and $\alpha(2\,2\,0)$, corresponding to α-phase Ta with $(1\,1\,0)$ orientation.

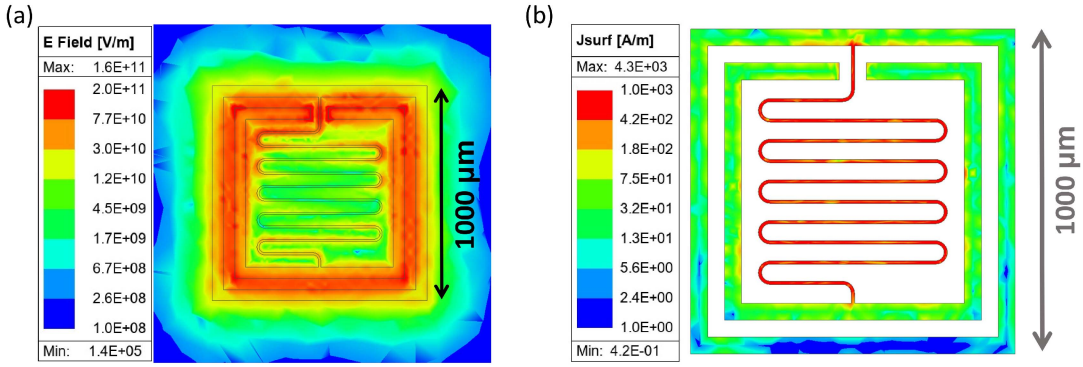

Fig. 10. HFSS simulation of (a) electric field distribution and (b) current distribution of Ta resonator. The length of the β phase grids is 5 μm. Surface impedance is calculated at 0.01 K. The simulated eigenfrequency is 5.5 GHz.

included in the residual loss Q_o which is extracted from the experiment data. The simulated electric field intensity distribution and current distribution are shown in Fig. 10.

Appendix G
Defect Phase Distribution in HFSS

Here, we show the defect phase distribution in the simulated resonator structure in HFSS in Fig. 11. For each defect concentration, the workflow generates a template. aedt file with the corresponding defect concentration and a specific defect distribution pattern. For each template file, the distribution pattern of defects is random. When performing a temperature-dependent quality factor simulation, the workflow implements it by copying the template file and assigning the surface impedance of the corresponding temperature to the defect grids and the nondefective part.

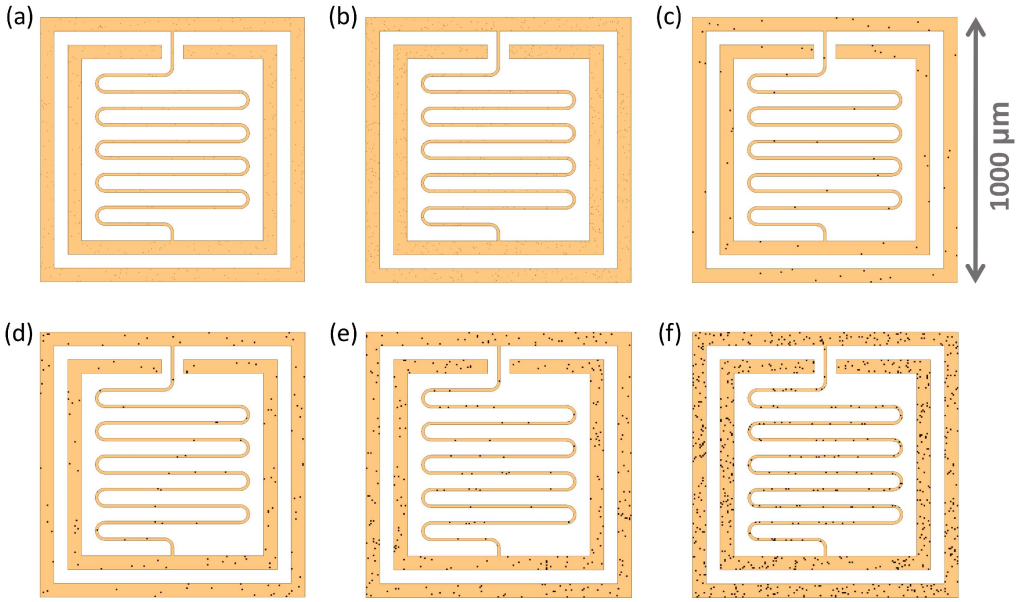

Fig. 11. Template distribution patterns of defect phase with different defect concentrations. (a)–(f) correspond to 0.1%, 0.2%, 0.5%, 1%, 2%, and 5%, respectively. To increase the speed of template file generation and reduce computational resource consumption during simulation, different defect grid sizes are used for different defect concentrations. For defect concentrations of 0.1% and 0.2%, the size of the defect grid is 1 μm; for the rest of defect concentrations, the size of the defect grid is 5 μm.

ACKNOWLEDGMENT

The authors are grateful to L. Radtke and S. Dehm for technical support. The authors are also grateful to A. Murani for fruitful discussion. The use of facilities was supported by the Karlsruhe Institute of Technology (KIT) Nanostructure Service Laboratory and the Karlsruhe Nano Micro Facility. The authors would like to acknowledge qKit for providing a convenient measurement software framework. The authors would also like to gratefully acknowledge the computing time provided on the high-performance computer HoreKa by the National High-Performance Computing Center, KIT. The authors would also like to acknowledge support by the state of Baden-Württemberg through bwHPC [48].

REFERENCES

[1] P. Krantz, M. Kjaergaard, F. Yan, T. P. Orlando, S. Gustavsson, and W. D. Oliver, "A quantum engineer's guide to superconducting qubits," *Appl. Phys. Rev.*, vol. 6, no. 2, Jun. 2019, Art. no. 021318.

[2] A. Blais, A. L. Grimsmo, S. M. Girvin, and A. Wallraff, "Circuit quantum electrodynamics," *Rev. Mod. Phys.*, vol. 93, no. 2, May 2021, Art. no. 025005.

[3] S. Kwon et al., "Gate-based superconducting quantum computing," *J. Appl. Phys.*, vol. 129, no. 4, 2021, Art. no. 041102.

[4] A. Krasnok, P. Dhakal, A. Fedorov, P. Frigola, M. Kelly, and S. Kutsaev, "Superconducting microwave cavities and qubits for quantum information systems," *Appl. Phys. Rev.*, vol. 11, no. 1, Jan. 2024, Art. no. 011302.

[5] S. E. Rasmussen et al., "Superconducting circuit companion—An Introduction with worked examples," *PRX Quantum*, vol. 2, no. 4, Dec. 2021, Art. no. 040204.

[6] A. P. M. Place et al., "New material platform for superconducting transmon qubits with coherence times exceeding 0.3 milliseconds," *Nat. Commun.*, vol. 12, no. 1779, pp. 1–6, 2021.

[7] C. Wang et al., "Towards practical quantum computers: Transmon qubit with a lifetime approaching 0.5 milliseconds," *NPJ Quantum Inf.*, vol. 8, no. 1, 2022, Art. no. 3.

[8] N. P. de Leon et al., "Materials challenges and opportunities for quantum computing hardware," *Science*, vol. 372, Apr. 2021, Art. no. 6539.

[9] Qiskit Development Team, Qiskit metal | quantum device design & analysis (Q-EDA) 0.1.5. Accessed: Sep. 18, 2025. [Online]. Available: https://qiskit-community.github.io/qiskit-metal/index.html

[10] M. F. Gely and G. A. Steele, "QuCAT: Quantum circuit analyzer tool in Python," *New J. Phys.*, vol. 22, no. 1, Jan. 2020, Art. no. 013025.

[11] T. Rajabzadeh, Z. Wang, N. Lee, T. Makihara, Y. Guo, and A. H. Safavi-Naeini, "Analysis of arbitrary superconducting quantum circuits accompanied by a Python package: SQcircuit," *Quantum*, vol. 7, Sep. 2023, Art. no. 1118.

[12] P. Groszkowski and J. Koch, "Scqubits: A Python package for superconducting qubits," *Quantum*, vol. 5, Nov. 2021, Art. no. 583.

[13] J. Johansson, P. Nation, and F. Nori, "QuTiP: An open-source Python framework for the dynamics of open quantum systems," *Comput. Phys. Commun.*, vol. 183, no. 8, pp. 1760–1772, 2012.

[14] J. Gao, J. Zmuidzinas, A. Vayonakis, P. Day, B. Mazin, and H. Leduc, "Equivalence of the effects on the complex conductivity of superconductor due to temperature change and external pair breaking," *J. Low Temp. Phys.*, vol. 151, no. 1, pp. 557–563, 2008.

[15] Z. K. Minev, I. M. Pop, and M. H. Devoret, "Planar superconducting whispering gallery mode resonators," *Appl. Phys. Lett.*, vol. 103, no. 14, 2013, Art. no. 142604.

[16] C. A. T. Garcia et al., "Disentangling superconductor and dielectric microwave losses in submicrometer Nb/SiO_2 interconnects using a multimode microstrip resonator," *Phys. Rev. Appl.*, vol. 21, 2024, Art. no. 024056, doi: 10.1103/PhysRevApplied.21.024056.

[17] V. Belitsky, C. Risacher, M. Pantaleev, and V. Vassilev, "Superconducting microstrip line model studies at millimetre and sub-millimetre waves," *Int. J. Infrared Millimeter Waves*, vol. 27, no. 6, pp. 809–834, 2006, doi: 10.1007/s10762-006-9116-5.

[18] G. Catelani and J. P. Pekola, "Using materials for quasiparticle engineering," *Mater. Quantum Technol.*, vol. 2, no. 1, Feb. 2022, Art. no. 013001.

[19] Kreiner et al., "In preparation,".

[20] Z. Yao, M. Sandberg, D. W. Abraham, and D. J. Bishop, "Low-loss liquid metal interconnects for superconducting quantum circuits," *Appl. Phys. Lett.*, vol. 124, no. 26, 2024, Art. no. 264002.

[21] J. Halbritter, "Fortran-program for the computation of the surface impedance of superconductors," Inst. Exp. Nucl. Phys., Karlsruhe Inst. Technol., Karlsruhe, Germany, KIT External Rep. KFK-Ext.03/70-06, 1970.

[22] J. Bardeen, L. N. Cooper, and J. R. Schrieffer, "Theory of superconductivity," *Phys. Rev.*, vol. 108, pp. 1175–1204, 1957.

[23] D. C. Mattis and J. Bardeen, "Theory of the anomalous skin effect in normal and superconducting metals," *Phys. Rev.*, vol. 111, 1958, Art. no. 412.

[24] J. Turneaure, "Microwave measurements on the surface impedance of superconducting tin and lead," Ph.D. dissertation, Phys. Dept., Stanford Univ., Stanford, CA, USA, 1966.

[25] R. Poepel, "Surface impedance and reflectivity of superconductors," *J. Appl. Phys.*, vol. 66, pp. 5950–5957, 1989.

[26] A. A. Abrikosov, L. P. Gorkov, and I. E. Dzyaloshinski, *Methods of Quantum Field Theory in Statistical Physics*. North Chelmsford, MA, USA: Courier Corporation, 1964.

[27] J. Halbritter, "Zur oberflaechenimpedanz von supraleitern," Ph.D. dissertation, Institut für Experimentelle Kernphysik (EKP), Karlsruhe Inst. Technol., Karlsruhe, Germany, 1969.

[28] F. Valenti et al., "Interplay between kinetic inductance, nonlinearity, and quasiparticle dynamics in granular aluminum microwave kinetic inductance detectors," *Phys. Rev. Appl.*, vol. 11, 2019, Art. no. 054087, doi: 10.1103/PhysRevApplied.11.054087.

[29] K. D. Crowley et al., "Disentangling losses in tantalum superconducting circuits," *Phys. Rev. X*, vol. 13, 2023, Art. no. 041005.

[30] C. Kittel, *Introduction to Solid State Physics*. Hoboken, NJ, USA: Wiley, 2024.

[31] D. Rieger, S. Günzler, M. Spiecker, A. Nambisan, W. Wernsdorfer, and I. Pop, "Fano interference in microwave resonator measurements," *Phys. Rev. Appl.*, vol. 20, 2023, Art. no. 014059.

[32] R Dhundhwal, "High quality superconducting tantalum resonators with beta phase defects," 2025, *arXiv:2502.17247*.

[33] T. van Schijndel et al., "Cryogenic growth of tantalum thin films for low-loss superconducting circuits," *Phys. Rev. Appl.*, vol. 23, 2024, Art. no. 034025.

[34] K. Kouwenhoven et al., "Resolving power of visible-to-near-infrared hybrid $\beta-\mathrm{Ta}/\mathrm{Nb}-\mathrm{Ti}-\mathrm{N}$ kinetic inductance detectors," *Phys. Rev. Appl.*, vol. 19, 2023, Art. no. 034007.

[35] H. Ibach and H. Lüth, *Festkörperphysik*. Berlin, Germany: Springer.

[36] J. Halbritter, "Comparison between measured and calculated RF losses in the superconducting state," *Zeitschrift für Physik*, vol. 238, pp. 466–476, 1970.

[37] "Technical data for tantalum," Accessed: Sep. 18, 2025. [Online]. Available: https://periodictable.com/Elements/073/data.html

[38] N. Klein et al., "The effective microwave surface impedance of high TC thin films," *J. Appl. Phys.*, vol. 67, no. 11, pp. 6940–6945, 1990, doi: 10.1063/1.345037.

[39] J. P. Turneaure, J. Halbritter, and H. A. Schwettman, "The surface impedance of superconductors and normal conductors: The Mattis-Bardeen theory," *J. Supercond.*, vol. 4, pp. 341–355, 1991.

[40] T. Greytak and J. Wernick, "The penetration depth in several hard superconductors," *J. Phys. Chem. Solids*, vol. 25, pp. 535–542, 1964.

[41] J. J. Hauser and H. C. Theuerer, "Superconducting tantalum films," *Rev. Mod. Phys.*, vol. 36, pp. 80–83, 1964.

[42] Y.-H. Lin et al., "Proximity-effect-induced anisotropic superconductivity in a monolayer Ni-Pb binary alloy," *ACS Appl. Mater. Interfaces*, vol. 14, no. 20, pp. 23990–23997, 2022.

[43] J. Kim, V. Chua, G. A. Fiete, H. Nam, A. H. MacDonald, and C.-K. Shih, "Visualization of geometric influences on proximity effects in heterogeneous superconductor thin films," *Nature Phys.*, vol. 8, no. 6, pp. 464–469, 2012.

[44] S. Kirkpatrick, "Percolation and conduction," *Rev. Modern Phys.*, vol. 45, 1973, Art. no. 574.

[45] D. S. McLachlan, M. A. G. Blaszkiewicz, and R. E. Newnham, "Electrical resistivity of composites," *J. Amer. Ceram. Soc.*, vol. 73, pp. 2187–2203, 1990.

[46] A. Gurevich and T. Kubo, "Surface impedance and optimum surface resistance of a superconductor with an imperfect surface," *Phys. Rev. B*, vol. 96, 2017, Art. no. 184515, doi: 10.1103/PhysRevB.96.184515.

[47] "Hochleistungsrechner Karlsruhe (Horeka)." Accessed: Sep. 18, 2025. [Online]. Available: https://www.scc.kit.edu/dienste/horeka.php

[48] "bwunicluster 2.0," Accessed: Sep. 18, 2025. [Online]. Available: https://www.scc.kit.edu/dienste/bwUniCluster_2.0.php